IEEE Open Journal of
Power Electronics

Received 5 August 2024; accepted 27 August 2024. Date of publication 30 August 2024;
date of current version 9 September 2024. The review of this article was arranged by Associate Editor Chandan Kumar.

Digital Object Identifier 10.1109/OJPEL.2024.3452169

Detailed Analysis of Optimized Pulse Patterns Interacting With Salient PMSMs Applying Different Symmetry Conditions

MAXIMILIAN HEPP [1], KIM KAISER[1], MICHAEL SAUR [1], AND MARK-M. BAKRAN [2] (Senior Member, IEEE)

[1]Power Electronics Advanced Development Department, Mercedes-Benz AG, 71059 Sindelfingen, Germany
[2]Department of Mechatronics, Centre for Energy Technology, University of Bayreuth, 95447 Bayreuth, Germany

CORRESPONDING AUTHOR: MAXIMILIAN HEPP (e-mail: maximilian.m.hepp@mercedes-benz.com).

ABSTRACT Efficiency and power density of electric vehicle drive systems are important metrics for their performance evaluation. To address these aspects, Optimized Pulse Patterns (OPPs) can be integrated into the modulation strategy. This research investigates the effects of OPPs on the current distortion of salient permanent magnet synchronous motors (PMSMs) applying different symmetry conditions. It places a particular emphasis on three-pulse switching within the overmodulation region. A mathematical model of salient PMSMs is used to demonstrate that the voltage phase angle significantly influences current harmonics. It is revealed that even with a low number of pulses, satisfactory sinusoidal currents can be achieved at high voltage phase angles, thereby reducing the inverter's switching efforts while preserving current waveform quality. Different waveforms such as quarter- and half-wave symmetry (QWS), unrestricted half-wave symmetry (HWS) and restricted HWS are compared, with an innovative approach proposed for unrestricted HWS. The benefits and drawbacks of these waveforms in application to salient PMSMs are investigated, with emphasis on the overmodulation region. It is noted that HWS shows benefits over QWS at medium-load operating points and when zero-vectors are in the waveforms. In contrast, no significant advantages of HWS over QWS could be identified in the overmodulation region. The research proposes a practical OPP implementation strategy that balances effort and efficiency based on this knowledge. Unlike previous studies that used random initial angles to explore solutions, this study methodically examines the solution space for HWS and QWS, selecting initial angles that enhance the chances of finding the global optimum.

INDEX TERMS Optimized pulse pattern, permanent magnet synchronous machines (PMSMs), pulse width modulation, synchronous modulation, variable speed drives.

I. INTRODUCTION

Optimized pulse patterns (OPPs) are well known in industrial drives and railway applications using induction motors connected to two-level voltage source inverters (VSI) [1]. Recent publications on OPPs are increasingly focusing on electric vehicle applications in combination with salient permanent magnetic synchronous machines (PMSMs) [2], [3], [4], [5], Fig. 1. In this context, the boundary conditions such as machine types, inverters, microcontrollers, and control architecture are different from those in industrial and railway applications. In industrial applications, OPPs are used to reduce and optimize the switching losses of IGBT inverters [6]. In automotive traction applications, OPPs are used to reduce motor and system losses [7], [8] and to optimize additional aspects such as the DC-link current stress [9], NVH [10], [11] or EMC behaviour [12].

Efficiency and power density are key performance indicators of electric vehicle traction drive trains. One way to address both, is to apply modulation strategies to increase the modulation index m for higher voltage utilization [13], [14]. This can be easily done by applying OPPs [15]. These are inherently capable of addressing the overmodulation region. They extend the linear modulation ($m \leq 1.15$, related to $\frac{u_{DC}}{2}$, where u_{DC} is the DC-link voltage) up to six-step modulation

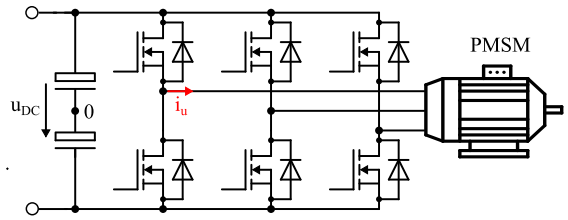

FIGURE 1. Electrical drive setup as used for example in electrical vehicles. Two-level VSI connected to a salient PMSM. Using OPPs the harmonic distortion of the phase currents, e.g i_u, can be reduced.

($m \approx 1.273$). Especially the overmodulation region II ($1.21 < m \leq 1.273$) is important, since the overmodulation region I ($1.15 < m \leq 1.21$) is phase conservative and can be accessed with space-vector pulse width modulation (SVPWM) [13]. The higher voltage utilization in the field-weakening region of electrical machines results in a lower current requirement to produce the same mechanical power compared to linear modulation strategies. Consequently, this leads to a reduction in both copper and iron losses [16], [17] within the machine. For the same rated current, the apparent output power (measured in kVA) of the VSI and thus the power density continue to increase as the voltage utilization is enhanced.

A. STATE-OF-THE-ART

Commonly the switching angles of the respective waveforms are calculated offline to match or optimize one or more of the previously named criteria. The state of the art is to optimize for low harmonic distortion of the (weighted) voltage supplied to the electrical machine [1], [18]. For induction machines, this correlates linearly with the current and flux harmonics, respectively.

For salient PMSMs, the voltage harmonics interact with the position-dependent inductances. Therefore, the current harmonics must be calculated using an accurate machine model of PMSMs [19], [20], [21], [22]. Considering the specific machine and its application, e.g. a non-sinusoidal back-EMF [23] or uncertainties in parameters [24] may be taken into account to refine the existing models and enhance the optimization of switching angles. Especially for automotive traction drives, the non-linear saturation characteristics of salient PMSMs can be considered [25].

During an electric period, with $\gamma_{el} \in [0, 2\pi]$ being the electrical angle of the machine, symmetry conditions are usually applied to the voltage waveforms and switching angles. This leads to a reduction of the complexity and inherently eliminates even harmonics. Half-wave symmetry (HWS) and quarter- and half-wave symmetry (QWS) conditions and their effect on optimization have been studied in various publications when optimizing voltage or current harmonics in induction machines only [26], [27], [28], [29].

The requirement of meeting the QWS condition is eased in [26], [27] for two-level inverter fed induction motor drives, and in [28], [29], [30] for three-level inverter fed induction motor drives This results in enhanced solutions using HWS depending on the modulation index.

When optimizing current harmonics for salient PMSMs, less research is available on symmetry conditions. In [31] it was found that HWS rather than QWS gives better results when optimizing current harmonics for salient PMSMs. However, no deeper insights are available and there is no explicit explanation of the valid operating range for this statement.

Although the overmodulation region is of particular importance for traction drives in vehicles, existing literature lacks an investigating the symmetry conditions for the overmodulation region with an emphasis on PMSMs. While six-step modulation achieves maximum voltage utilization, drawbacks such as high DC-link voltage ripple or high torque ripple prevent its use in a wide operational range of electric vehicles. However, it is easy to implement on automotive microcontrollers [13]. Pulse numbers greater than three can be difficult to implement because automotive microcontrollers usually lack the computational performance and proper timer peripherals. Thus, OPPs with a pulse number of three are particularly important for automotive powertrains. The modulation index can be seamlessly adjusted within the overmodulation range, thereby enabling 95-100% of the voltage utilization, depending on the boundary conditions of the DC-link or the NVH performance. In recent literature this is addressed by [13], [15]. However, symmetry conditions or salient PMSMs are not explicitly considered.

Furthermore, the formulations given in the named publications are less specific about the relationship between the desired voltage phase angle θ_u and the inherent phase of the fundamental wave of the pulse pattern. A different interpretation of unrestricted HWS and restricted HWS is possible when this relationship is taken into account.

In existing publications, there is less focus on the optimization itself. The solution space is usually explored by local optimization algorithms like MATLAB's fmincon [32] in combination with random starting angles to find the optimal solution [20], [21], [25], [28], [29]. Examples of the solution space for OPPs are given in [1], [18], but only for QWS waveforms regarding the optimization of induction machines. However, a proper knowledge of the solution space is needed to find the best possible solutions, especially when working with random initialization angles and local optimization algorithms.

In summary, the following research opportunities have been identified:

- investigating OPPs and their symmetries for salient PMSMs within the relevant overmodulation region ($1.15 < m \leq 1.273$) to increase efficiency and power density for automotive drive trains.
- putting a focus on OPPs with a pulse number of three for a realizable implementation on microcontrollers and seamless access to the overmodulation region. In this context, an understanding of the solution space would be advantageous for identifying the optimal solutions for the lowest current harmonics.

TABLE 1 Content of Existing Literature in Comparison to the Research Presented Here

Literature	OPPs	HWS	Saliency	Overmodulation
[13], [15]	✓			✓
[14]				✓
[19]–[25]	✓		✓	
[26]–[30]	✓	✓		
[31]	✓	✓	✓	
This research	✓	✓	✓	✓

B. CONTRIBUTION

In order to address the mentioned research opportunities, this paper presents a comprehensive examination of optimized pulse patterns for salient PMSMs and their symmetry conditions, with a particular focus on the overmodulation region. Table 1 clarifies that, in contrast to the existing literature, a holistic view of the mentioned topics is provided.

This paper extends prior research by showing that the current harmonics are strongly dependent on the voltage phase angle when a distinct saliency is present. A higher voltage phase angle inherently reduces current harmonics.

Zero-vector properties of QWS and HWS waveforms are explained and analysed regarding the overmodulation region.

Based on this knowledge, it can be shown that even three-pulse switching or six-step modulation is sufficient to ensure minimal distortion of the generated currents, depending on the operating point. An operational strategy for OPPs is derived. It is specifically tailored to electric vehicle applications. Thus, a realizable implementation on microcontrollers and seamless access to the overmodulation region is possible.

Various symmetry conditions of QWS and HWS are elaborated in detail. A distinct interpretation of unrestricted HWS is derived, for which multiple redundant solutions exist that lead to the same current distortion.

This provides an interpretable visualization of the solution space for the current harmonics of a salient PMSM with respect to three-pulse switching. Understanding the configuration of the solution space enhances the probability of identifying the global minimum by employing appropriate initial values for the optimization process. An extrapolation to higher pulse numbers is feasible based on this foundation. The impact of both QWS and HWS on the current harmonics of salient PMSMs can be explored within this defined solution space.

C. PAPER STRUCTURE

The paper is organized as follows: Section II gives an overview of synchronous modulation and OPPs for salient PMSMs. Emphasis is placed on the explanation of HWS. The zero vector properties, which influence the current distortion in the overmodulation region, are explained. The influence of QWS and HWS on the current harmonics is observed regarding salient PMSMs. Section III provides an insight into the solution space and the optimization itself. Section IV presents the results of the optimization and discusses the obtained findings. In Section V, measurements are performed to validate the model on which the proposed theory is based. Section VI concludes the paper.

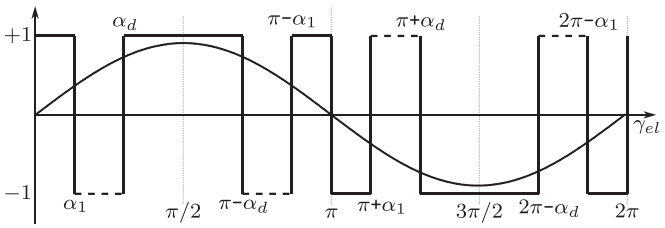

FIGURE 2. QWS Type-A waveform and its fundamental (not to scale).

II. SYNCHRONOUS MODULATION FOR PMSM DRIVES

A. WAVEFORM REPRESENTATION - MACHINE PHASE VOLTAGES

When OPPs are applied to a VSI, inherently synchronous modulation is used. The number of synchronous pulses $q := f_{\mathrm{sw}}/f_{\mathrm{el}}$, the quotient of the switching frequency f_{sw} and the electrical frequency f_{el}, is an integer. The switching angles $\boldsymbol{\alpha} = [\alpha_1, \alpha_2, \ldots, \alpha_d]$ define the synchronous pulse pattern, where d is the number of independent switching angles. The value of d depends on the pulse number q and the symmetry conditions.

For synchronous modulation the waveform can be easily represented by a Fourier series expansion with the Fourier coefficients a_0, a_ν and b_ν:

$$f(\gamma_{\mathrm{el}}) = \frac{a_0}{2} + \sum_{\nu=1}^{\infty} a_\nu \sin(\nu\gamma_{\mathrm{el}}) + b_\nu \cos(\nu\gamma_{\mathrm{el}}) \qquad (1)$$

By applying symmetry conditions to the pulse pattern, such as QWS ($f(\gamma_{\mathrm{el}}) = f(\pi - \gamma_{\mathrm{el}})$ and $f(\gamma_{\mathrm{el}}) = -f(\pi + \gamma_{\mathrm{el}})$, $d = \frac{q-1}{2}$, Fig. 2) or HWS ($f(\gamma_{\mathrm{el}}) = -f(\pi + \gamma_{\mathrm{el}})$, $d = q - 1$) the DC component a_0 and the even harmonics are naturally eliminated and only the odd harmonics exist. However, for full-wave symmetry ($f(\gamma_{\mathrm{el}}) = f(\gamma_{\mathrm{el}} + 2\pi)$, $d = 2q$) this is generally not the case and the DC component a_0 as well as the even harmonics exist. For this reason, and because of the additional complexity due to the higher degrees of freedom, full-wave symmetry is not discussed in detail in this publication.

In the following, only QWS and HWS are examined, so $a_0 = 0$ and $\nu = 2k + 1$ for $k \in \mathbb{N}_0$. The Fourier representation of the machine phase voltages is then given in (2) containing only odd and non-triple harmonics ν, since triple harmonics are additionally canceled out in balanced, star-connected

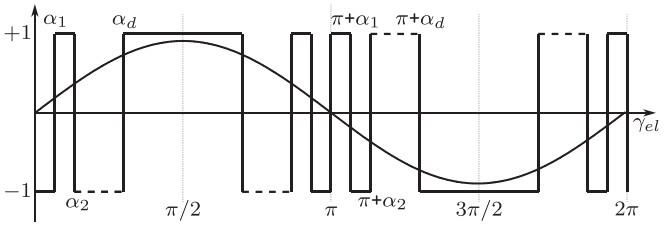

FIGURE 3. QWS Type-B waveform and its fundamental (not to scale).

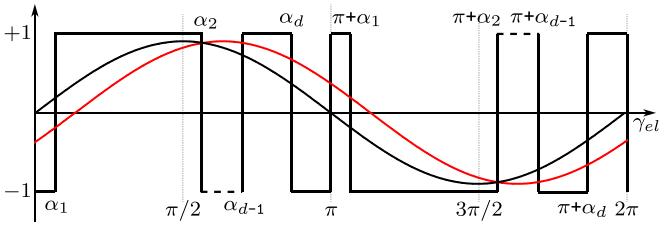

FIGURE 4. Restricted HWS Type-B waveform (——). In the unrestricted case (——) switching does not necessarily occur at the zero crossings of the fundamental and a Type-A and Type-B waveform can not be distinguished anymore.

three-phase systems [33]. u_{DC} is the DC link voltage.

$$\begin{bmatrix} u_{\mathrm{u}}(\boldsymbol{\alpha}) \\ u_{\mathrm{v}}(\boldsymbol{\alpha}) \\ u_{\mathrm{w}}(\boldsymbol{\alpha}) \end{bmatrix} = \frac{u_{\mathrm{DC}}}{2} \sum_{\nu=1,5,7\ldots}^{\infty} \begin{bmatrix} a_\nu(\boldsymbol{\alpha})\cos\left(\nu\left(\gamma_{\mathrm{el}}+\varphi\right)\right) \\ a_\nu(\boldsymbol{\alpha})\cos\left(\nu\left(\gamma_{\mathrm{el}}+\varphi-\frac{2\pi}{3}\right)\right) \\ a_\nu(\boldsymbol{\alpha})\cos\left(\nu\left(\gamma_{\mathrm{el}}+\varphi-\frac{4\pi}{3}\right)\right) \end{bmatrix} + \begin{bmatrix} b_\nu(\boldsymbol{\alpha})\sin\left(\nu\left(\gamma_{\mathrm{el}}+\varphi\right)\right) \\ b_\nu(\boldsymbol{\alpha})\sin\left(\nu\left(\gamma_{\mathrm{el}}+\varphi-\frac{2\pi}{3}\right)\right) \\ b_\nu(\boldsymbol{\alpha})\sin\left(\nu\left(\gamma_{\mathrm{el}}+\varphi-\frac{4\pi}{3}\right)\right) \end{bmatrix} \tag{2}$$

The Fourier coefficients $a_\nu(\boldsymbol{\alpha})$ and $b_\nu(\boldsymbol{\alpha})$ are calculated with (3) for QWS and (4) for HWS respectively. Two types of waveforms can be distinguished: Namely one where (+) is applied in (3) and (4) and the waveform starts with a rising edge when the fundamental phase voltage crosses zero into the positive half-wave (Type-A waveform), Fig. 2. One where (−) is applied where the waveform starts with a falling edge (Type-B waveform) when the fundamental phase voltage crosses zero into the positive half-wave, Fig. 3. For HWS, however, a meaningful distinction between the waveforms is just possible by setting $a_1 = 0$ or $b_1 = 0$, see Fig. 4. This specific waveform is also known as restricted HWS, which will be explained at the end of this Section. Otherwise the zero-crossing of the fundamental wave is neither located at a rising nor a falling edge (unrestricted HWS) and the sign in (4) can be neglected. For better display, the argument $(\boldsymbol{\alpha})$ is omitted in the following.

$$\left.\begin{aligned} a_\nu(\boldsymbol{\alpha}) &= 0 \\ b_\nu(\boldsymbol{\alpha}) &= \pm\tfrac{4}{\nu\pi}\left(1+2\textstyle\sum_{i=1}^{d}(-1)^i\cos(\nu\alpha_i)\right) \end{aligned}\right\} \tag{3}$$

$$\left.\begin{aligned} a_\nu(\boldsymbol{\alpha}) &= \pm\tfrac{4}{\nu\pi}\textstyle\sum_{i=1}^{d}(-1)^{i+1}\sin(\nu\alpha_i) \\ b_\nu(\boldsymbol{\alpha}) &= \pm\tfrac{4}{\nu\pi}\left(\underbrace{1}_{\tilde{c}}+\textstyle\sum_{i=1}^{d}(-1)^i\cos(\nu\alpha_i)\right) \end{aligned}\right\} \tag{4}$$

The desired voltage fundamental wave of the pulse pattern can be specified by the amplitude $|\vec{u}_{\mathrm{dq}}|$ and the voltage phase angle θ_{u}:

$$\begin{bmatrix} u_{\mathrm{u},1} \\ u_{\mathrm{v},1} \\ u_{\mathrm{w},1} \end{bmatrix} = |\vec{u}_{\mathrm{dq}}| \begin{bmatrix} \cos\left(\gamma_{\mathrm{el}}+\theta_{\mathrm{u}}\right) \\ \cos\left(\gamma_{\mathrm{el}}+\theta_{\mathrm{u}}-\frac{2\pi}{3}\right) \\ \cos\left(\gamma_{\mathrm{el}}+\theta_{\mathrm{u}}-\frac{4\pi}{3}\right) \end{bmatrix}. \tag{5}$$

In the rotating dq-reference frame θ_{u} can be calculated by $\theta_{\mathrm{u}} = \mathrm{atan2}(\frac{u_{\mathrm{q},0}}{u_{\mathrm{d},0}})$, where $u_{\mathrm{d/q},0}$ are the DC dq-voltages.

If only the fundamental components of the phase voltages are considered, (2) can be represented as (6):

$$\begin{bmatrix} u_{\mathrm{u},1} \\ u_{\mathrm{v},1} \\ u_{\mathrm{w},1} \end{bmatrix} = \frac{u_{\mathrm{DC}}}{2} \begin{bmatrix} \sqrt{a_1^2+b_1^2}\cos\left(\gamma_{\mathrm{el}}+\varphi-\mathrm{atan2}\left(\frac{b_1}{a_1}\right)\right) \\ \sqrt{a_1^2+b_1^2}\cos\left(\gamma_{\mathrm{el}}+\varphi-\mathrm{atan2}\left(\frac{b_1}{a_1}\right)-\frac{2\pi}{3}\right) \\ \sqrt{a_1^2+b_1^2}\cos\left(\gamma_{\mathrm{el}}+\varphi-\mathrm{atan2}\left(\frac{b_1}{a_1}\right)-\frac{4\pi}{3}\right) \end{bmatrix} \tag{6}$$

The introduction of the angle φ in (2) and thus the phase shift of the waveforms is mandatory in order to ensure that the position of the corresponding fundamental phase voltages $u_{\mathrm{u/v/w},1}$ is identical to that specified by its angle θ_{u}, if (5) and (6) are compared. As a consequence, the correlation

$$\varphi = \theta_{\mathrm{u}} + \frac{\pi}{2} \tag{7}$$

results in case of QWS ($a_\nu = 0$), whereas in the general case of HWS the condition

$$\varphi = \theta_{\mathrm{u}} + \mathrm{atan2}\left(\frac{b_1}{a_1}\right) \tag{8}$$

applies.

The relationship between the angles φ and θ_{u} can be visualized based on the waveforms and the corresponding fundamental phase voltages, as shown in Fig. 5 for phase u. Without the presence of the phase shift introduced by φ and given a QWS, the zero crossing of the fundamental phase voltage is always located at the first edge of the corresponding waveform, as can be derived from (5)–(7). In this case, it is necessary to restrict b_1 to positive values only, in order to ensure that the fundamental phase voltage starts with the positive half-wave and, consequently, to distinguish correctly between Type-A and Type-B waveforms. When describing the fundamental phase voltages as cosine functions according to (5) and (6), the initial position is therefore always shifted by $\frac{\pi}{2}$.

However, this is not necessarily the case for HWS. Due to the degree of freedom given by the possibility of a non-zero

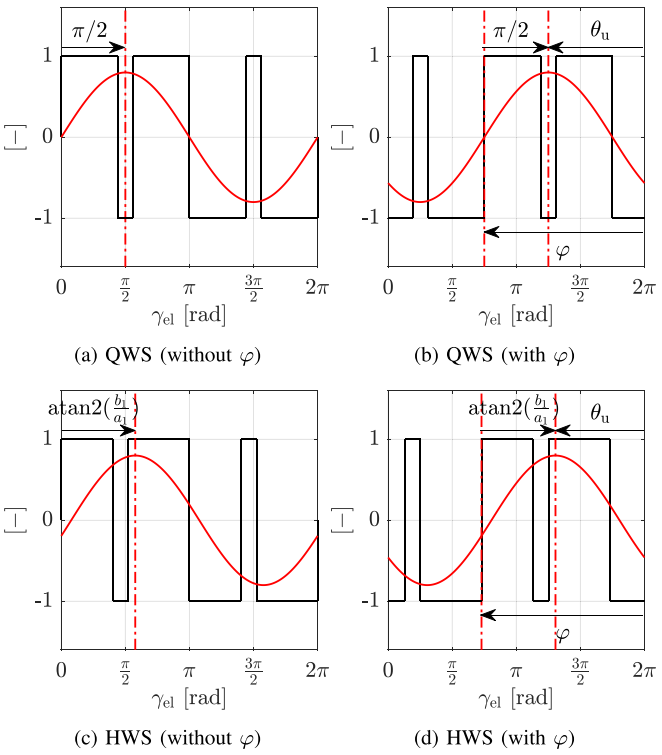

FIGURE 5. Visualization of the occurring phase shift for QWS and HWS with and without the introduction of the additional angle φ.

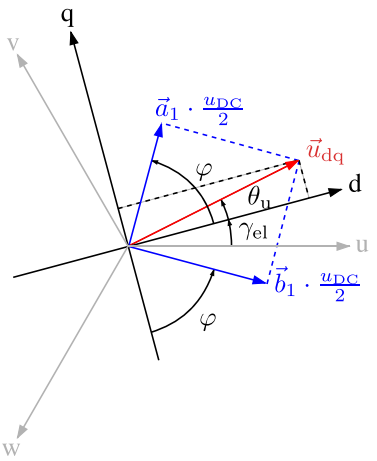

FIGURE 6. Representation and decomposition of the fundamental voltage vector in the dq-reference frame.

a_1, the zero crossing of the fundamental phase voltage can be located arbitrarily, as can be seen in Fig. 5. Hence, the initial phase shift can generally be described by atan2($\frac{b_1}{a_1}$).

Taking (5) and (6) into account, the resulting fundamental voltage vector can be visualized in the dq-reference frame, as can be seen in Fig. 6. A decomposition into two orthogonal vectors, $\vec{a}_1$ and $\vec{b}_1$ respectively, can be performed, which represent the corresponding Fourier coefficients of the fundamental phase voltages. In this context, φ denotes the angle

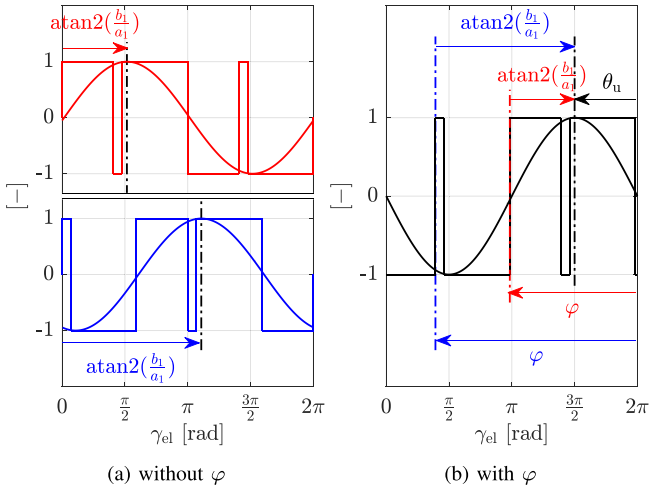

FIGURE 7. Redundant waveforms and corresponding fundamental phase voltages before and after the respective phase shift due to the angle φ.

between $\vec{b}_1$ and the negative q-axis as well as the angle between $\vec{a}_1$ and the positive d-axis. In the case of QWS and thus $a_1 = 0$, $\vec{b}_1$ is always aligned with the fundamental voltage vector $\vec{u}_{dq}$.

With the introduction of the phase angle φ for the general HWS case, q redundant waveforms exist. These waveforms have the same fundamental and the same harmonic spectrum, but different switching angles shifted by q different φ. Fig. 7 shows two of three solutions with an arbitrary $|\vec{u}_{dq}|$ and arbitrary θ_u for $q = 3$. This will be further illustrated and explained in Section III.

The most general form of HWS ($a_1 \neq 0\,, b_1 \neq 0$), as investigated in this paper, is also denoted as non-restricted, unrestricted, generalized or shifted HWS in the scientific literature [34], [35], [36]. The naming refers to the fact that the zero crossings of the fundamental phase voltages do not necessarily have to be located at edges of the corresponding waveforms, see Fig. 4. However, this specific restraint can be enforced by specifying a_1 as zero, which is further referred to as restricted HWS in the literature.

The dependency of the angle φ on the Fourier coefficients a_1 and b_1 in the case of unconstrained HWS and thus the need of a corresponding look-up table (LUT) for φ can be completely avoided if the $\tilde{c}$ part in (4) is omitted and $d := q$ as well as $a_1 = 0$ holds true. Nevertheless, it depends on the implementation approach of the modulator whether it is more advantageous to store an additional switching angle or φ. In the following φ is used and $d := q - 1$ applies. This allows a simple interpretable visualisation of the solution space for the current harmonics of a salient PMSM regarding a pulse number of $q = 3$.

B. ZERO-VECTOR PROPERTIES FOR TYPE-A AND TYPE-B WAVEFORMS

Specifically for QWS, additional characteristics can be identified for Type-A and Type-B waveforms regarding zero

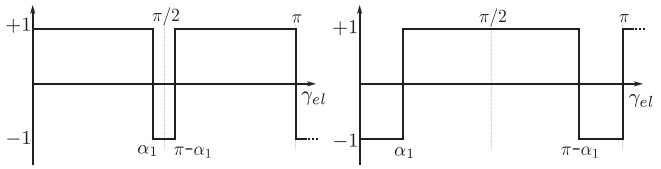

(a) Type-A (b) Type-B

FIGURE 8. Different QWS waveforms for $q = 3$. Just the positive halfwave is displayed.

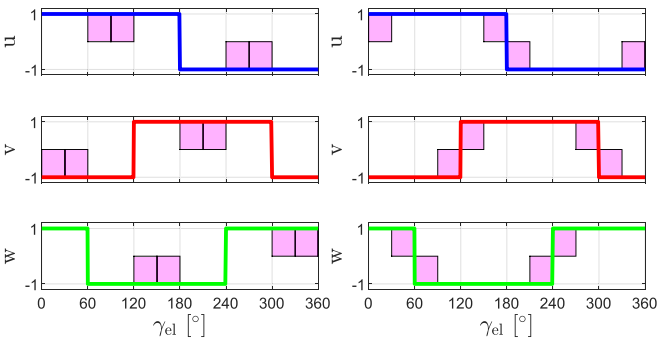

(a) Type-A (b) Type-B

FIGURE 9. Three-phase pulse pattern for $q = 3$ with different QWS symmetry conditions. The region where switching actions can meaningfully take place is defined by the highlighted pink areas.

vectors. To the best of the authors' knowledge, these characteristics have not been discussed in literature yet. However, they help to understand the results discussed in Section IV. In the following, mainly pulse patterns with $q = 3$ will be discussed, Fig. 8. However, the results are also applicable to higher pulse numbers.

From the single-phase pulse pattern (Fig. 8), the three-phase pulse pattern can be easily derived, Fig. 9. The highlighted pink areas define the region where switching actions can occur meaningfully. Type-A is only defined for α_1 within the range of 60° to 90° for $q = 3$. $\alpha_1 > 30°$ for Type-B waveforms results in a discontinuous sequence with respect to the active space vectors for $q = 3$.

For the case $q = 3$, it is clear that the Type-A waveform inherently includes zero vectors to establish the desired modulation index, while the Type-B waveform does not for $\alpha_1 < 30°$. This characteristic can be further observed in the flux trajectory ψ in the $\alpha\beta$-plane of the corresponding pulse patterns, Fig. 10. The flux trajectory can be obtained by integrating the respective three-phase pulse patterns.

From the flux trajectory alone, it is clear that there are significant differences in the flux harmonics, and consequently the current harmonics, depending on whether or not the waveform contains zero vectors. Specifically, at higher modulation indices ($m > 1.21$, overmodulation region II), the flux trajectory without zero vectors tends to approximate a circle, whereas this is not the case at lower modulation indices. Here, the distortion of the flux is more pronounced compared to waveforms that include zero vectors.

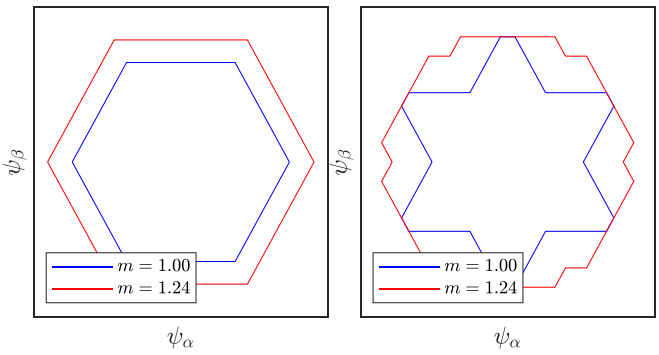

(a) Type-A (b) Type-B

FIGURE 10. Flux trajectory for $q = 3$ with different QWS symmetry conditions. The flux trajectory can be obtained by integrating the respective three-phase pulse patterns.

For pulse numbers with odd degrees of freedom, such as $q = 3$ ($d = 1$), the same conclusions can be extended to higher pulse numbers for $m > 1.21$ (overmodulation region II). Conversely, for pulse numbers with even degrees of freedom, such as $q = 5$ ($d = 2$), Type-A waveforms lack zero vectors, while Type-B waveforms inherently contain them for $m > 1.21$ (overmodulation region II).

C. SALIENT PMSM MODEL - MACHINE PHASE CURRENTS

A general model including non-linear magnetic behaviour of a PMSM in the dq-reference frame is given in (9) [37]. R_s is the stator resistance of the machine and ψ_p the flux of the permanent magnet, L_x are the absolute inductances, L_{xx} the differential inductances and i_x are the currents in the dq-reference frame. The dependences of the current i_d and i_q of the inductances are dropped for simplicity in the following.

$$\begin{bmatrix} u_d \\ u_q \end{bmatrix} = \begin{bmatrix} R_s & -\omega_{el} L_q\left(i_d, i_q\right) \\ \omega_{el} L_d\left(i_d, i_q\right) & R_s \end{bmatrix} \begin{bmatrix} i_d \\ i_q \end{bmatrix} + \begin{bmatrix} L_{dd}\left(i_d, i_q\right) & L_{dq}\left(i_d, i_q\right) \\ L_{qd}\left(i_d, i_q\right) & L_{qq}\left(i_d, i_q\right) \end{bmatrix} \frac{\mathrm{d}}{\mathrm{d}t} \begin{bmatrix} i_d \\ i_q \end{bmatrix} + \begin{bmatrix} 0 \\ \psi_p \omega_{el} \end{bmatrix} \tag{9}$$

Using synchronous modulation, the harmonic RMS-content can be calculated considering the non-linear magnetic behaviour. The PMSM parameters are listed in Table 2.

In order to facilitate an analytical derivation, the following simplifications must be assumed for the modelling process:

- the stator resistance (e.g., here $R_s = 12\,\mathrm{m\Omega}$) has a negligible impact on the current harmonics. Thus, $R_s = 0\,\mathrm{m\Omega}$ is assumed.
- the flux linkage ψ_p contains no harmonics, hence it does not influence the current harmonics.
- the cross-coupling inductances L_{dq} and L_{qd} are neglected, since they are small compared to L_{dd} and L_{qq} ($L_{dq} = L_{qd} < 30$ micro; H depending on the operating point).

TABLE 2 Parameters of the PMSM

Parameter	Value
pole pairs z_p	4
stator resistance R_s	12 mΩ at 25°C
nominal flux linkage ψ_p	153 mWb at 25°C
nominal absolute inductance L_d / L_q	387 / 748 μH
nominal differential inductance L_dd / L_qq	387 / 748 μH
nominal mech. speed n_{nom}	4500 rpm
maximum mech. speed n_{max}	9000 rpm

- the motor parameters do not depend on the stator or rotor temperature and are assumed as constant for stationary operating points.
- the flux tables, and therefore the inductances, are determined and measured at one specific speed. It is assumed that these values remain constant over different speeds.
- interlocking time of the semiconductors and the ohmic voltage drop in the inverter is neglected since fast switching, low $R_\mathrm{ds,on}$ SiC inverters are used for automotive traction drives.

The phase voltages u_uvw described by (2) can be transformed to u_d and u_q by using a Park-Clarke transformation. In the next step, the obtained dq-voltages described by a Fourier series expansion can be inserted into (9) and solved for the current harmonics $i_{\mathrm{dq},n}$. Using the inverse Park-Clarke transformation $i_{\mathrm{u},n}$ can be obtained and the RMS value $i_{\mathrm{u},n,\mathrm{RMS}}$ can be calculated.

This process is conducted step by step in [25]. The present work refrains from such detailed exposition and instead only presents the RMS value, which, contrary to existing literature, has been reformulated to distinguish between isotropic and anisotropic components within the current harmonics, (10)–(12) ($k \in \mathbb{N}$).

$$\begin{aligned} G_n = {} & \frac{1}{\left(n^2 L_\mathrm{dd} L_\mathrm{qq} - L_\mathrm{d} L_\mathrm{q}\right)^2} \\ & \times \Big[\left((nL_\mathrm{dd} + L_\mathrm{d})^2 + \left(nL_\mathrm{qq} + L_\mathrm{q}\right)^2\right) \\ & \times \frac{1}{2}\left(a_{n-1}^2 + b_{n-1}^2\right) \\ & + \left((nL_\mathrm{dd} - L_\mathrm{d})^2 + \left(nL_\mathrm{qq} - L_\mathrm{q}\right)^2\right) \\ & \times \frac{1}{2}\left(a_{n+1}^2 + b_{n+1}^2\right) + G_\mathrm{saliency}\Big] \end{aligned} \tag{10}$$

$$\begin{aligned} G_\mathrm{saliency} = {} & \left(n^2\left(L_\mathrm{qq}^2 - L_\mathrm{dd}^2\right) + L_\mathrm{d}^2 - L_\mathrm{q}^2\right) \\ & \times \sqrt{a_{n+1}^2 + b_{n+1}^2} \cdot \sqrt{a_{n-1}^2 + b_{n-1}^2} \\ & \times \cos\left(2\theta_\mathrm{u} + 2 \cdot \mathrm{atan2}\left(b_1/a_1\right)\right. \\ & \left. + \mathrm{atan2}\left(b_{n-1}/a_{n-1}\right) - \mathrm{atan2}\left(b_{n+1}/a_{n+1}\right)\right) \end{aligned} \tag{11}$$

$$i_{\mathrm{u},n,\mathrm{RMS}} = \frac{u_\mathrm{DC}}{\sqrt{2} \cdot 2\,\omega_\mathrm{el}} \underbrace{\sqrt{\sum_{n=6k}^{\infty} G_n}}_{\sigma} \tag{12}$$

To reduce the harmonic content of the phase currents $i_{\mathrm{u},n,\mathrm{RMS}}$, the switching angles $\boldsymbol{\alpha}$ have to be selected in a way that σ is minimal:

$$\begin{aligned} & \sigma_\mathrm{opt}(\boldsymbol{\alpha}) = \min\, \sigma(\boldsymbol{\alpha}) \\ & \text{subject to} \\ & m\frac{u_\mathrm{DC}}{2} = |\vec{u}_\mathrm{dq}| = \frac{u_\mathrm{DC}}{2} \cdot \sqrt{a_1^2(\boldsymbol{\alpha}) + b_1^2(\boldsymbol{\alpha})} \\ & 0 < \alpha_1 < \alpha_2 < \ldots < \alpha_d < \frac{\pi}{2} \quad \text{for QWS} \\ & 0 < \alpha_1 < \alpha_2 < \ldots < \alpha_d < \pi \quad \text{for HWS} \end{aligned} \tag{13}$$

where m is the modulation index. As solver for the optimization problem MATLAB's fmincon is used. The optimization process itself is explained in Section III.

D. INTERACTION OF QWS AND HWS WITH SALIENT PMSMS

For PMSMs with no saliency (or induction machines), $G_\mathrm{saliency} = 0$. For machines with saliency, $G_\mathrm{saliency} \neq 0$ applies and lower σ can be obtained using HWS instead of QWS. However, the following explanation highlights that HWS outperforms QWS only within a specific operational range.

Applying QWS, (11) simplifies to (14) since $a_\nu = 0$:

$$\begin{aligned} G_\mathrm{saliency} = {} & \left(n^2\left(L_\mathrm{qq}^2 - L_\mathrm{dd}^2\right) + L_\mathrm{d}^2 - L_\mathrm{q}^2\right) \\ & \times |b_{n+1}| \cdot |b_{n-1}| \cdot (-\cos(2\theta_\mathrm{u})) \end{aligned} \tag{14}$$

The (14) shows that the harmonic content of salient PMSMs depends on the voltage phase angle and thus on the torque of the machine. The relationship between torque and voltage phase angle can be expressed as (15) for salient PMSMs if the resistive voltage drop is ignored [38]. In the following, only motor operation will be of interest, but the conclusions are also valid for generator operation, see Fig. 11(a).

$$\begin{aligned} T_\mathrm{EM} = {} & -\frac{3z_\mathrm{p}}{4}\left(\frac{\psi_\mathrm{PM}}{L_\mathrm{d}} \cdot \frac{u_\mathrm{DC}\, m \cos(\theta_\mathrm{u})}{\omega_\mathrm{el}}\right. \\ & \left. + \frac{L_\mathrm{d} - L_\mathrm{q}}{L_\mathrm{d} L_\mathrm{q}} \cdot \frac{u_\mathrm{DC}^2\, m^2 \sin(2\theta_\mathrm{u})}{4\,\omega_\mathrm{el}^2}\right) \end{aligned} \tag{15}$$

For the simplest case of QWS, the six-step modulation, $q = 1$, $\boldsymbol{\alpha} = [\ ]$ and $b_\nu = \frac{4}{\nu\pi}$. So the switching frequency f_sw is equal to the electrical fundamental frequency f_el. The resulting values for σ are shown in Fig. 11(b) using the PMSM parameters listed in Table 2. The harmonic content in the phase currents is reduced in the high torque range using six-step operation. Above 180° voltage phase angle, the harmonic

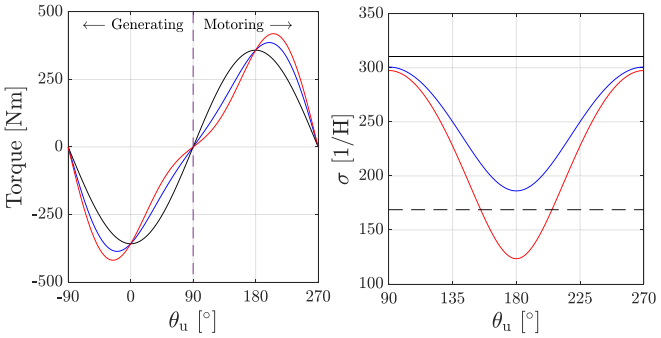

(a) Torque vs θ_u curve

(b) σ for six-step operation vs θ_u in the motoring region

FIGURE 11. (a) Torque of a salient PMSM with the parameters given in Table 2 (——) at 6000 rpm, $u_{DC} = 640\,V$ and $m = 1.15$. Additionally, the results are given for a non-salient PMSM (——) and a PMSM with $2 \cdot L_q$ and nominal L_d (——). (b) current harmonic content represented by σ using six-step operation (nominal values (——), no saliency ($L = L_d$) (——), no saliency ($L = L_q$) (- - -), $2 \cdot L_q$ and nominal L_d (——).

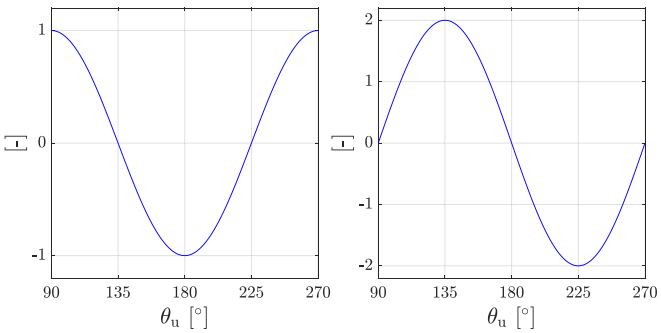

(a) $-\cos(2\theta_u)$ for motor operation

(b) derivative of $\cos(2\theta_u)$

FIGURE 12. Curve of $-\cos(2\theta_u)$ and its derivative. The harmonics are inherently reduced by $-\cos(2\theta_u)$ in PMSMs with saliency. HWS can further reduce the harmonics, especially where the derivative is greatest. When the derivative is close to zero, HWS has little advantage over QWS.

content increases again. The curve follows that of $-\cos(2\theta_u)$ according to (14), see Fig. 12(a). In the high torque range of a salient PMSM, the switching losses of the inverter can be reduced while still maintaining good quality in the current waveform using six-step modulation. With higher saliency, the reduction of harmonics is more pronounced, while for non-salient machines the effect cannot be used.

For QWS and $q = 3$, the single degree of freedom is used to adjust the switching angles to set the desired modulation index. The b_n's in (14) cannot be tuned to minimize harmonics. For higher pulse numbers q, i.e. higher degrees of freedom, the reduction of harmonics is possible to a certain extent, while keeping the general form of $-\cos(2\theta_u)$.

When using HWS instead of QWS, (11) applies, and the cosine function in (11) can additionally be used to reduce harmonics, since a_ν and b_ν are arguments of the cosine. The derivative of $\cos(2\theta_u)$ describes the effect of the Fourier coefficients on the result of the cosine function, see Fig. 12(b). When θ_u is close to 90° or close to 180°, the derivative is almost 0, so small changes in a_ν and b_ν have little effect on the result. When θ_u is about 135°, the derivative reaches its maximum. Small adjustments to the Fourier coefficients have the largest effect on the cosine function. Thus, the improvement from using HWS instead of QWS is expected to follow the general shape of the derivative as shown in Fig. 12(b). Since the function $-\cos(2\theta_u)$ has its minimum at 180°, no benefit of HWS over QWS is expected at this point.

It can be shown that using restricted HWS for $q = 3$, one degree of freedom is used to set the desired modulation index, while the other degree of freedom is used to set $a_1 = 0$. This gives the same result as QWS.

A comparison and summary of the discussed waveforms is given in Table 3.

III. OPTIMIZATION OF THE PULSE PATTERNS

The higher the number of pulses q, the more degrees of freedom d are available, the more complex the solution space becomes, and thus the computational complexity increases. MATLAB's fmincon is a gradient-based optimization algorithm, and thus convergence and reasonable performance of the optimization process depend on an adequate choice of initial values for the respective switching angles. For higher pulse numbers this becomes increasingly difficult. In the literature this has been done using random values (100 are used in [29], [39], [40], 1000 in [20]) for each operating point. In the following, more detailed considerations are made for a pulse number of $q = 3$ to increase the probability of finding the global minimum.

Considering QWS, the corresponding objective function $\sigma(\boldsymbol{\alpha})$ depends only on a single switching angle α_1 to be varied and can be visualized according to Fig. 13(a). It can be seen that the global minimum is located at 60°, so for the corresponding waveform there is an alternation between positive and negative pulses of equal length, which in turn is accompanied by a modulation index of $m = 0$. This exact point defines the boundary between the ranges that distinguish the occurrence of a Type-A or Type-B waveform. For each type, the switching angle α_1 provides the only degree of freedom, so the feasible region associated with an arbitrary modulation index m to be satisfied is uniquely specified by discrete points along the objective function, see Fig. 13(a).

Using a gradient-based optimization method such as MATLAB's fmincon with random initial values, it is likely that no feasible solution will be found when optimizing, for example, a QWS Type-A waveform with initial angles between 0° and 60°. Instead, a proper initialization for $q = 3$ would be $\alpha_1 \in \{0, 45°, 90°\}$ applied in three optimization cycles. So for $q = 3$ and higher pulse numbers the following initialization angles are suggested:

- all permutations of the set $\{0°, 45°, 90°\}$ with respect to $\alpha_1 \leq \alpha_2 \leq \ldots \leq \alpha_d$ to find the initial angles at the corners and edges of the solution space (e.g. $\alpha_1 \in \{0°, 45°, 90°\}$ for $q = 3$; $(\alpha_1|\alpha_2) \in \{(0|0)°, (0|45)°, (0|90)°, (45|45)°, (45|90)°, (90|90)°\}$ for $q = 5$).

TABLE 3 Different Symmetry Conditions Compared

Symmetry	Eq. for a_ν, b_ν	Eq. for φ	d	Zero-vectors present	Benefits	Drawbacks
QWS Type-A	(3), using $+$	(7)	$\frac{q-1}{2}$	$q = 3, 7, 11, \ldots$ for $m > 1.21$	• $\frac{q-1}{2}$ angles to be stored	• Results for σ are inferior to HWS, depending on m and θ_u
QWS Type-B	(3), using $-$	(7)	$\frac{q-1}{2}$	$q = 5, 9, 13, \ldots$ for $m > 1.21$	• $\frac{q-1}{2}$ angles to be stored	• Results for σ are inferior to HWS, depending on m and θ_u
HWS restricted	(4), $\tilde{c} = 1$, $a_1 = 0$ (4), using $+$ for Type-A (4), using $-$ for Type-B	(7)	$q-1$	depending on m	• Better results for σ than QWS for $q > 3$ depending on m and θ_u	• Same results as QWS for $q = 3$ • Both, Type-A and Type-B waveforms must be optimized to find the best solution • $q-1$ angles need to be stored
HWS unrestricted	(4), $\tilde{c} = 0$, $a_1 = 0$	(7)	q	depending on m	• Better results for σ than QWS for $q > 1$ depending on m and θ_u	• q angles need to be stored • Optimization with q degrees of freedom
	(4), $\tilde{c} = 1$, $a_1 \neq 0$	(8)	$q-1$	depending on m	• Better results for σ than QWS for $q > 1$ depending on m and θ_u • More likely to find optimal solution for having q redundant pulse patterns	• $q-1$ angles and φ need to be stored

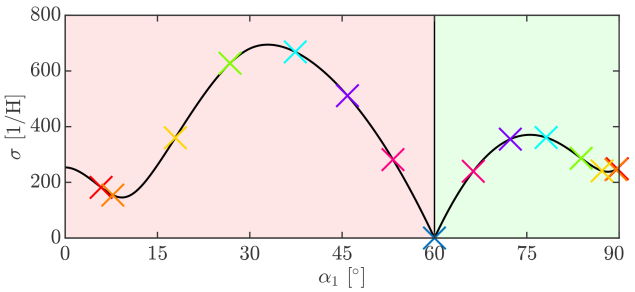

(a) QWS

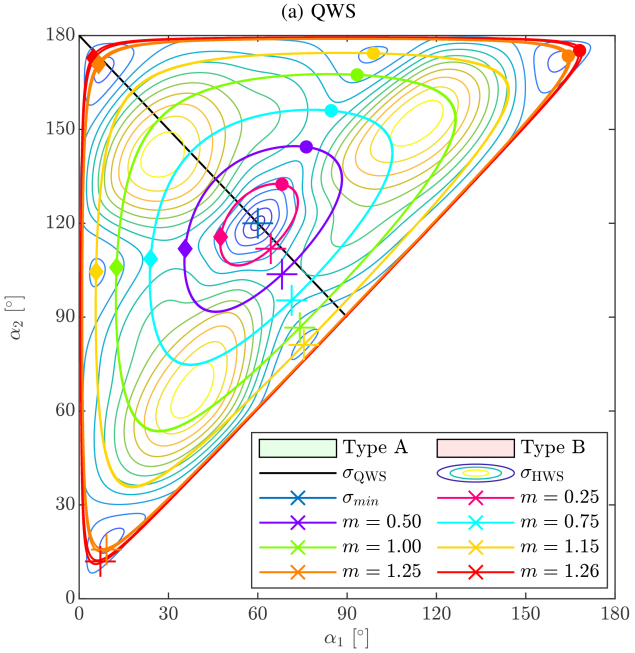

(b) HWS

FIGURE 13. Solution space of $\sigma(\alpha)$ using (12) for QWS (a) and HWS (b) with $q = 3$, $\theta_\mathbf{u} = 130°$ and nominal inductances. For HWS, q redundant solutions exist. These solutions are distinguished by different marker styles.

- a uniform distribution of switching angles between 0° and 90° (e.g. $\alpha_1 = 45°$ for $q = 3$; $\alpha_1 = 30°$, $\alpha_2 = 60°$ for $q = 5$) to locate the initial angles between the corners of the solution space.
- two neighbouring, already optimized switching angle sets are taken as initial values to locate the initial angles close to already found optima. (e.g. using the solutions $\boldsymbol{\alpha}(m = 1.20, \theta_\mathrm{u} = 90°)$ and $\boldsymbol{\alpha}(m = 1.19, \theta_\mathrm{u} = 100°)$ for the optimization $\boldsymbol{\alpha}(m = 1.20, \theta_\mathrm{u} = 100°)$)

Since both Type-A and Type-B waveforms must be considered, the optimization must be performed twice to select the best result.

In the case of HWS, two degrees of freedom are available, α_1 and α_2 respectively, and the objective function can be represented by contour lines as shown in Fig. 13(b). It can be observed that the previously discussed solution space of Fig. 13(a) is included as a subset, which is generally valid regardless of the specified pulse number, since the QWS can always be considered as a special case of the HWS. In accordance with the previous discussion of QWS, the global minimum of the objective function $\sigma(\boldsymbol{\alpha})$ lies at $(\alpha_1, \alpha_2) = (60°, 120°)$. Due to the additional degree of freedom introduced by the angle α_2 to be varied, the feasible region associated with an arbitrary modulation index m – in contrast to QWS – takes on the appearance of closed curves, as shown in Fig. 13(b).

As mentioned in Section II-A, there are q pulses that start with a rising edge or a falling edge, resulting in q different possibilities in terms of the waveform being shifted by the phase φ. This results in q redundant solutions for each value of the modulation index m, resulting in the same pulse pattern and thus current distortion. In Fig. 13(b) this is shown for $q = 3$, where different solutions are highlighted with different markers.

Considering the occurrence of different local maxima in the solution space, the optimization process is also performed several times with an appropriate set of different initial values for the switching angles as in the QWS case. Permutations from the set $\{0, 90°, 180°\}$ can be chosen for the initial values of the switching angles, but due to the higher number of switching angles to be varied, $(q-1)$, this leads to a higher computational effort and will not be used in the following. Instead, analogous optimization results can be obtained by choosing the following initial values:

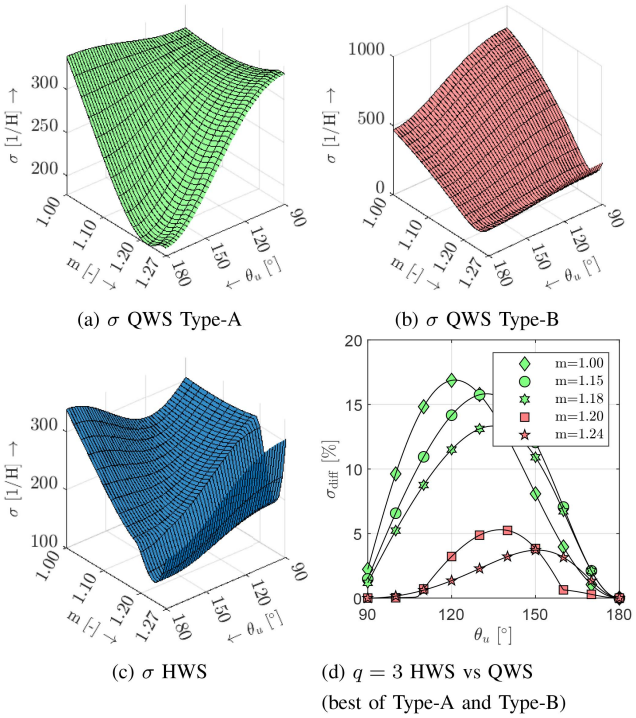

(a) σ QWS Type-A (b) σ QWS Type-B

(c) σ HWS (d) $q = 3$ HWS vs QWS (best of Type-A and Type-B)

FIGURE 14. Results of the optimization for $q = 3$. (a) QWS Type-A is applied. (b) QWS Type-B is applied. (c) HWS is applied. (d) improvement using HWS compared to best QWS results (Type-A ——, Type-B ——).

- using the angles resulting from the best QWS solution, Type-A or Type-B, as mentioned above, since it can be seen from Fig. 13(b) that the HWS solution is close to the one obtained by QWS.
- a uniform distribution of switching angles between 0° and 180° (e.g. $\alpha_1 = 60°$, $\alpha_2 = 120°$ for $q = 3$; $\alpha_1 = 36°$, $\alpha_2 = 72°$, $\alpha_3 = 108°$, $\alpha_4 = 144°$ for $q = 5$) to locate the initial angles between the corners of the solution space.
- two neighbouring, already optimized switching angle sets are taken as initial values to locate the initial angles close to already found optima. (e.g. using the solutions $\boldsymbol{\alpha}(m = 1.20, \theta_u = 90°)$ and $\boldsymbol{\alpha}(m = 1.19, \theta_u = 100°)$ for the optimization $\boldsymbol{\alpha}(m = 1.20, \theta_u = 100°)$)

In addition, this approach ensures that the optimization process for HWS always produces the same or better solutions than in the case of QWS.

IV. RESULTS AND DISCUSSION

A. OPTIMIZATION RESULTS FOR THREE-PULSE SWITCHING

The results obtained using (13) and the optimization procedure described in the previous section are shown in Fig. 14 for $q = 3$. Similar results are obtained using an extensive search with 1000 random initial values, indicating that the proposed optimization procedure yields nearly identical solutions.

In Fig. 14 the results for the motoring operation $\theta_u \in [0°, 180°]$ and for the modulation index $m \in [1, \frac{4}{\pi}]$ are displayed. For many applications, such as drive trains for electric vehicles, SVPWM or discontinues modulation (DPWM) would be used for $m > 1$, since lower total losses could be achieved in this operating range using the modulation strategies mentioned [3].

QWS Type-A gives better results than using Type-B for $m = 1$ up to $m \approx 1.21$ (the beginning of the overmodulation II region). This result is expected and follows the conclusions from Section II-B. The results for HWS are a combination of those obtained by QWS Type-A and Type-B with improved results for σ depending on the voltage phase angle θ_u. The improvement σ_{diff} using HWS instead of QWS for different m is displayed in Fig. 14(d). Here, HWS is compared to the best result obtained by QWS σ_{QWS}, either by a Type-A or a Type-B waveform:

$$\sigma_{diff} = \frac{\sigma_{QWS} - \sigma_{HWS}}{\sigma_{QWS}} \cdot 100\%. \tag{16}$$

With a phase angle θ_u close to 90° or 180°, the solution obtained with HWS is basically the same as the one obtained with QWS. The greatest benefit of HWS can be achieved when θ_u is between 110° and 160°. The results and the advantage of HWS over QWS are as expected, see Section II-D. The general shape of the improvement follows the derivative of $\cos(2\theta_u)$. For $q = 3$ there is only a small advantage with HWS in the overmodulation region II ($m > 1.21$). For lower modulation and medium load operation, the current distortions can be reduced by 18% for the machine used. This again follows the conclusions from Section II-B, since the zero vector can be placed arbitrarily. For $q = 3$ Type-B naturally has no zero vectors (if $\alpha < 30°$), so the benefit of HWS is less than QWS.

This can also be illustrated in the solution space, Fig. 15. The solution space changes with different θ_u and - considering the current-dependent inductances $L_{d/q}$ and $L_{dd/qq}$ - with different currents depending on the operating point. However, the Fourier coefficients a_ν and b_ν for a given (α_1, α_2) point do not change, nor does the feasible range for a given modulation index. The phase angle θ_u is varied for $m = 1.15$. For θ_u close to 180° or 90°, the value of σ is nearly identical to that obtained by QWS.

B. OPTIMIZATION RESULTS FOR HIGHER PULSE NUMBERS

As shown in Fig. 16, the results from above are also true for $q \in \{5, 7\}$. For these pulse numbers, once again an extensive search with 1000 random initial values as well as the proposed optimization method mentioned in Section III is applied. Similar results are obtained, indicating again that correct solutions can be found applying the suggested initialization angles.

Discontinuities of σ_{diff} can be seen in Fig. 16. This can be observed exactly at the points where the Type-A QWS becomes better than the Type-B waveform, or vice versa.

From Fig. 16 it can be concluded that higher pulse numbers q also reduce the benefits of HWS.

Furthermore, within the overmodulation region II ($m > 1.21$), waveforms for $q \in \{5, 7\}$ without zero vectors yield optimal results for QWS. In this context, HWS also shows comparatively modest advantages.

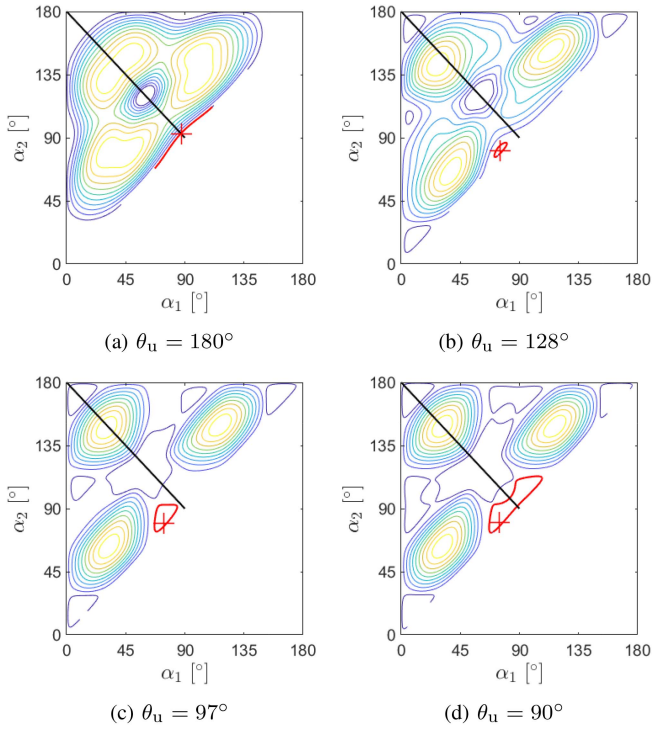

(a) $\theta_u = 180°$ (b) $\theta_u = 128°$

(c) $\theta_u = 97°$ (d) $\theta_u = 90°$

FIGURE 15. Objective function for different torque operating points with different voltage phase angles θ_u using $q = 3$ and $m = 1.15$. In the red encircled area the results are just up to 3% higher compared to the optimal solution marked with +. The black line marks the results that can be obtained by QWS.

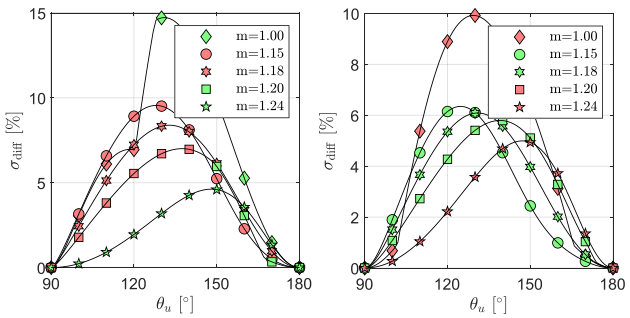

(a) $q = 5$ HWS vs QWS (best of Type-A and Type-B)

(b) $q = 7$ HWS vs QWS (best of Type-A and Type-B)

FIGURE 16. Improvement using HWS compared to best QWS results (Type-A ——, Type-B ——) for pulse numbers $q \in \{5, 7\}$.

C. IMPLEMENTATION STRATEGY BASED ON THE OBTAINED RESULTS

To obtain the actual RMS current distortion $i_{u,n,RMS}$ of a PMSM, (12) can be applied. Equation (12) shows that with higher electrical frequency ω_{el} (refers to mechanical speed) $i_{u,n,RMS}$ is reduced. Moreover, (11) illustrates that $i_{u,n,RMS}$ decreases with increasing voltage phase angle θ_u (refers to torque) in salient PMSMs.

Thus, even small pulse numbers such as $q = 3$ or six-step modulation can provide satisfactory values of $i_{u,n,RMS}$ when ω_{el} is high and/or θ_u is high.

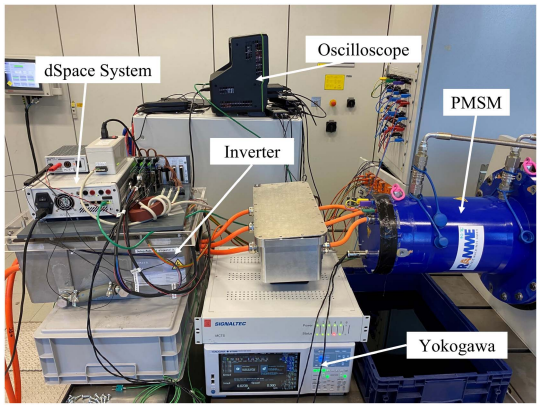

FIGURE 17. Test-bench measurement setup consisting of the PMSM with the parameters from Table 2 and a VSI based on SiC-MOSFETs.

Higher pulse numbers would lead to better values of $i_{u,n,RMS}$, but are challenging to implement in automotive traction drives due to the limited resources of microcontrollers. These limitations encompass computational capacity, memory allocation, and peripheral components such as timers. For this reason, pulse numbers greater than three will not be further considered in the following discussion.

In combination with the results obtained in Section IV-A, this knowledge results to the proposal of an operational strategy for implementing OPPs in PMSMs of electric vehicles:

1) HWS should be used primarily at low modulation indices ($m < 1.15$). However, in this modulation range, OPPs, especially $q = 3$, would not be used in electric vehicle applications [3], [41].
2) At low or very high θ_u, HWS has minimal advantages over QWS. Memory and/or computation on the microcontroller can be saved in these areas of operation.
3) To access the overmodulation region II OPPs can be applied. Especially in this context, QWS without zero vector gives good results, such that HWS offers only marginal advantages. In a practical application, the additional complexity of HWS would therefore be avoided.
4) At very high ω_{el} (which corresponds to the mechanical speed) and especially under high voltage phase angle conditions (refers to torque), six-step modulation or three-pulse switching can be applied, since the current distortion in salient PMSMs is already very low due to the high speeds and high voltage angles.

V. EXPERIMENTAL VALIDATION

A. EXPERIMENTAL TEST BENCH SETUP

To confirm the validity of the model (10), the advantages of HWS over QWS and the statements made in the previous sections, measurements are made on a machine test bench.

In Fig. 17 the test bench setup is illustrated. A SiC inverter is connected to 250 kW PMSM with the parameters from Table 2.

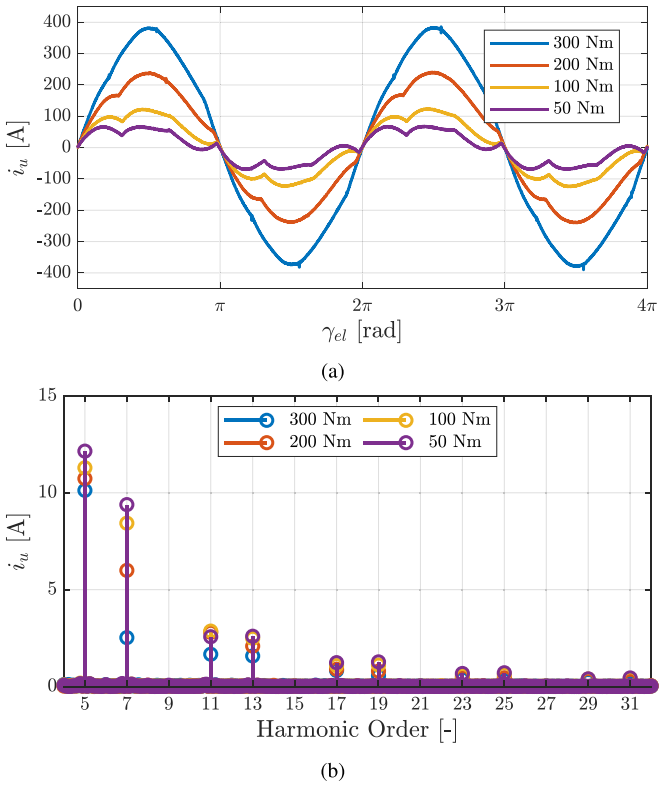

FIGURE 18. Measurement results to validate the current distortion reduction by a higher voltage phase angle. (a) Six-step modulation is used to acquire the phase current i_u over a range of torque levels when the motor is running at a speed of 7000 rpm. (b) FFT of the phase current i_u.

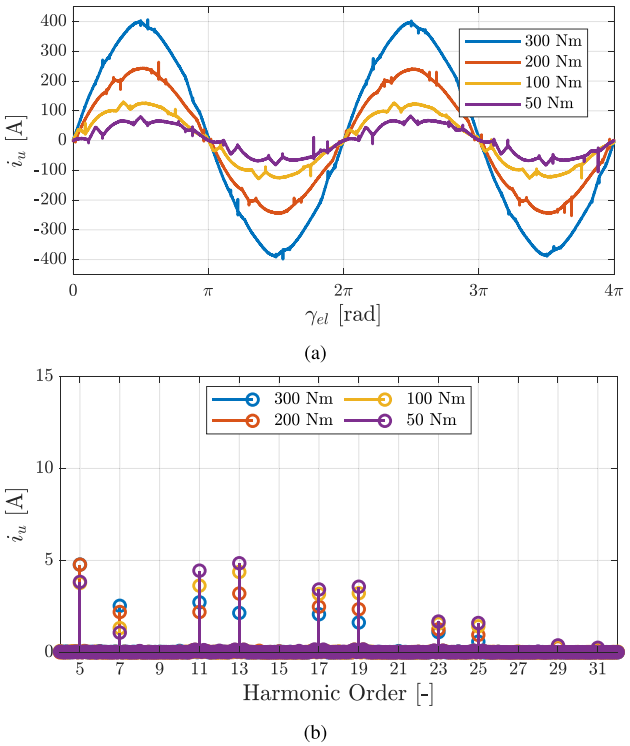

FIGURE 19. Measurement results to validate the current distortion reduction by a higher voltage phase angle. (a) OPPs with $q = 3$ and $m = 1.24$ are used to acquire the phase current i_u over a range of torque levels when the motor is running at a speed of 7000 rpm. (b) FFT of the phase current i_u.

A high-bandwidth LeCroy MDA810A oscilloscope is used to obtain the DC-link voltage and the Drain-Source voltages of the three high-side switches with 120 MHz differential probes. The AC-phase currents are measured with 30 MHz Rogowski coils. All signals are sampled with 10 MS/s. The mechanical output torque and the mechanical speed of the motor setup are measured using a HBM T12HP torque transducer connected to a Ýokogawa power analyser. The control is implemented on a dSpace MicroLabBox and the synchronous modulator is implemented on the MicroLabBox's field-programmable gate array (FPGA). The control algorithm used for applying OPPs is explained in detail in [41].

B. EXPERIMENTAL VALIDATION: CURRENT DISTORTION REDUCTION BY HIGHER VOLTAGE PHASE ANGLES

To validate the conclusions drawn from (14) and Fig. 11(b), six-step operation is applied to the machine at 7000 rpm and different torque set-points, see Fig. 18. The current waveform itself already indicates that at higher voltage phase angles (refers to higher torque), the current harmonics are reduced for salient PMSMs. This observation can be confirmed by examining the FFT. The RMS current distortion $i_{\mathrm{u,n,RMS}}$ is displayed in Fig. 20(a) and compared to the results obtained by simulation. In particular, the 7th harmonic is drastically reduced at higher load angles. Although six-step modulation

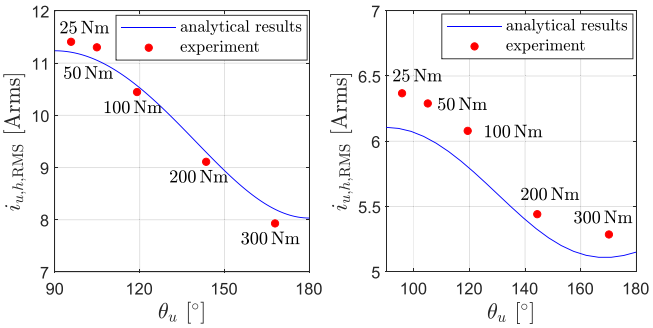

FIGURE 20. Comparison of experimental (——) and analytical ((12)) results (——) for the same pulse patterns but applied with different voltage phase angles. For salient PMSMs an inherent reduction of the current distortion can be observed, applying higher voltage phase angles.

is used with a pulse number of $q = 1$, the current waveform remains nearly sinusoidal at 300 Nm. Increasing the pulse number would result in higher switching losses, although the current waveform is already satisfactory. The general shape follows that expected in Fig. 11(b).

The same experiment is also conducted for OPPs with $q = 3$ applying QWS. The modulation index for this experiment is $m = 1.24$, addressing the overmodulation region II at

7000 rpm. Again the current waveforms, Fig. 19(a), and the FFT, Fig. 19(b), show the same effect as for six-step modulation regarding lower current distortions at higher voltage phase angles (refers to higher torque) for salient PMSMs. The RMS current distortion $i_{\mathrm{u,n,RMS}}$ is displayed in Fig. 20(b) and compared to the results obtained by simulation. Once again, the results show that currents with low distortions can be achieved at high voltage phase angles with significantly low pulse numbers or switching frequencies respectively.

Experimental and analytical results match quite well, despite some deviations arising from model inaccuracies and simplifications as stated in Section II-C.

C. EXPERIMENTAL VALIDATION: QWS VS HWS FOR DIFFERENT VOLTAGE PHASE ANGLES AND THREE-PULSE SWITCHING

Further experimental investigations will now be carried out to determine whether the previous findings regarding the advantages HWS over QWS in terms of modulation index and voltage angle are correct.

For $q = 3$, different modulation indices ($m \in \{1.15, 1.18, 1, 20, 1.24\}$) are applied alongside various torque set points to the PMSM. HWS waveforms and QWS waveforms are utilized, and the corresponding current harmonics are measured. Depending on m the QWS waveform with the lowest current disortion is used: Type-A for $m \in \{1.15, 1.18\}$ and Type-B for $m \in \{1.20, 1.24\}$, see Fig. 14(d).

σ_{diff} is calculated from the experimental results obtained and compared to the theoretical ones, Fig. 21(a)–(d). As expected from Fig. 14(d) and the theoretical derivation in Section II-D, the advantage of HWS over QWS is minimal at both low and high voltage phase angles (refers to torque). The same is true for higher modulation indices, especially $m = 1.24$, representing the overmodulation region II.

Table 4 shows the comparison of the experimental and theoretical current distortions for different m. Again, a good agreement can be observed, despite small deviations arising from effects the model does not take into account, see Section II-C.

Additionally, selected current waveforms are displayed in Figs. 22–25. Within these figures, QWS and HWS are compared, along with their corresponding FFTs. Waveforms for small voltage phase angles (30 Nm) and medium voltage phase angles (120 Nm) for $m = 1.15$ and $m = 1.24$ are selected. Visually, it is apparent that for linear modulation, HWS offers obvious benefits, while for the overmodulation region II, no visual difference can be discerned.

The results obtained by experiments prove that the HWS waveform has the greatest advantages over QWS in the medium load range, with a θ_{u} between 120° and 150°. In contrast, the advantages of HWS decrease when it is used in the low or high load range or in the overmodulation region. Thus, the previously proposed theory based on the PMSM model (10) is validated.

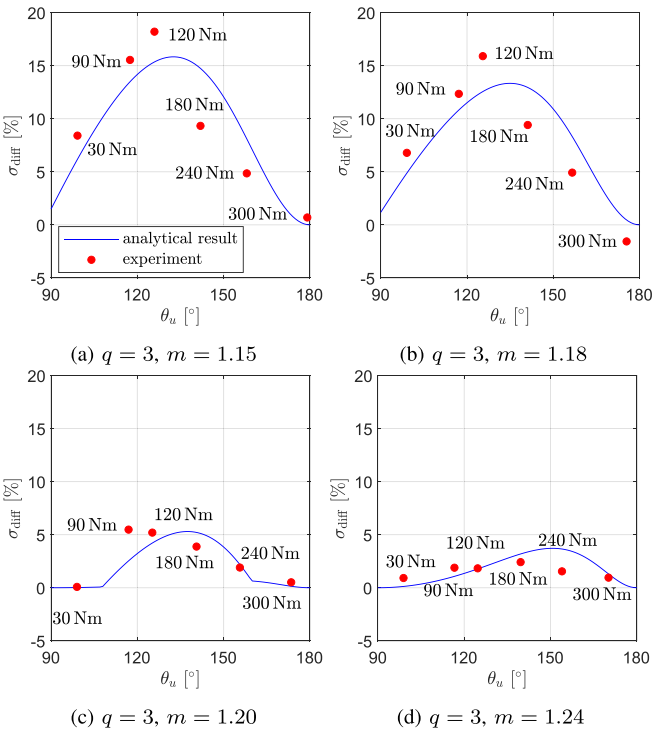

FIGURE 21. Comparison of experimental (——) and analytical (Eq. (12)) results (——). Different Torques ∈ {30, 90, 180, 240, 300} Nm applied to the PMSM at different modulation indices *m*. HWS waveforms and QWS waveforms are applied and the respective σ_{diff} is obtained.

TABLE 4 Comparison of Experimental and Analytical Results Applying (12) for Different θ_{u}, $q = 3$, and $m \in \{1.15, 1.18, 1, 20, 1.24\}$

q	m	Torque	θ_{u}	$i_{\mathrm{u,n,RMS}}$ [Arms]				σ_{diff} [%]	
				HWS		QWS			
	[-]	[Nm]	[°]	Eq. (12)	experiment	Eq. (12)	experiment	Eq. (12)	experiment
3	1.15	30	99.19	11.24	10.42	12.03	11.38	6.55	8.41
		90	117.46	9.83	9.05	11.41	10.71	13.87	15.54
		120	125.95	9.30	8.41	10.98	10.29	15.28	18.20
		180	141.96	8.76	8.81	10.21	9.71	14.24	9.32
		240	158.06	8.73	8.27	9.51	8.69	8.12	4.85
		300	179.10	8.93	9.54	8.94	9.61	0.01	0.69
3	1.18	30	99.08	11.49	10.67	12.12	11.45	5.15	6.78
		90	117.15	10.14	9.34	11.41	10.66	11.14	12.34
		120	125.49	9.54	8.57	10.90	10.19	12.51	15.89
		180	141.11	8.60	8.52	9.86	9.41	12.74	9.41
		240	156.57	8.22	7.85	8.95	8.26	8.13	4.92
		300	175.48	8.37	8.57	8.40	8.43	0.29	-1.56
3	1.20	30	99.01	11.44	11.68	11.44	11.69	0.02	0.08
		90	116.95	10.47	9.87	10.77	10.44	2.79	5.47
		120	125.21	9.83	9.73	10.28	10.27	4.41	5.19
		180	140.58	8.78	8.52	9.25	8.86	5.12	3.88
		240	155.66	8.20	7.65	8.36	7.80	1.96	1.90
		300	173.50	7.78	6.76	7.78	6.79	0.05	0.51
3	1.24	30	98.89	7.08	7.60	7.09	7.67	0.12	0.92
		90	116.60	6.74	6.63	6.82	6.76	1.08	1.89
		120	124.69	6.52	6.69	6.63	6.81	1.71	1.83
		180	139.61	6.12	6.13	6.28	6.28	2.61	2.34
		240	153.99	5.90	6.18	6.03	6.27	2.27	1.54
		300	170.18	5.84	5.59	5.87	5.65	0.54	0.95

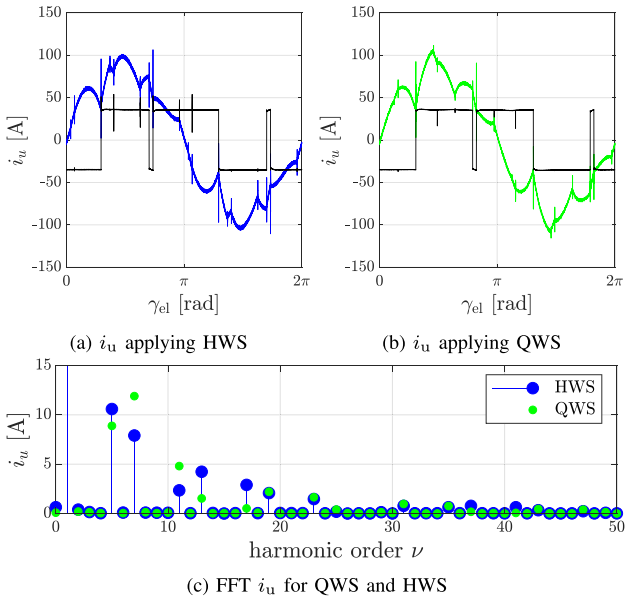

(a) i_u applying HWS (b) i_u applying QWS

(c) FFT i_u for QWS and HWS

FIGURE 22. Measured current waveforms and current FFTs applying QWS and HWS at $m = 1.15$ and $\theta_u = 99.19°$ (30 Nm) and 7000 rpm. Additionally the applied pulse pattern obtained by measurements is displayed (——). These measurements emphasizing the smaller benefits at $m = 1.15$ comparing HWS and QWS at small θ_u.

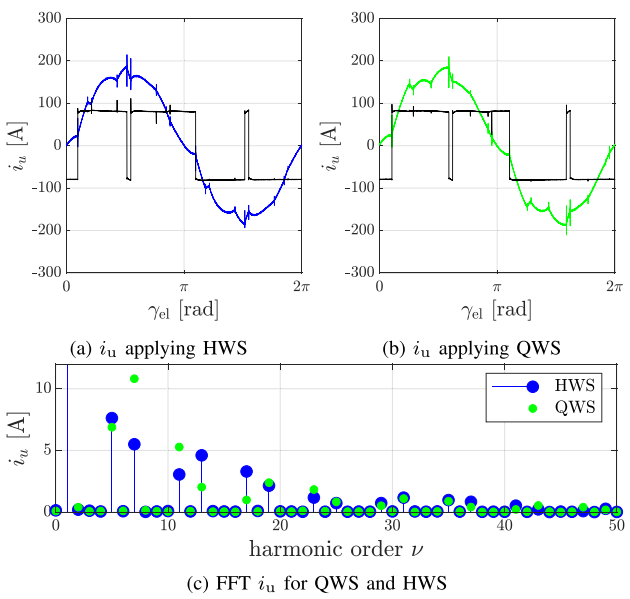

(a) i_u applying HWS (b) i_u applying QWS

(c) FFT i_u for QWS and HWS

FIGURE 23. Measured current waveforms and current FFTs applying QWS and HWS at $m = 1.15$ and $\theta_u = 125.95°$ (120 Nm) and 7000 rpm. Additionally the applied pulse pattern obtained by measurements is displayed (——). These measurements emphasizing the benefits at $m = 1.15$ comparing HWS and QWS at medium θ_u.

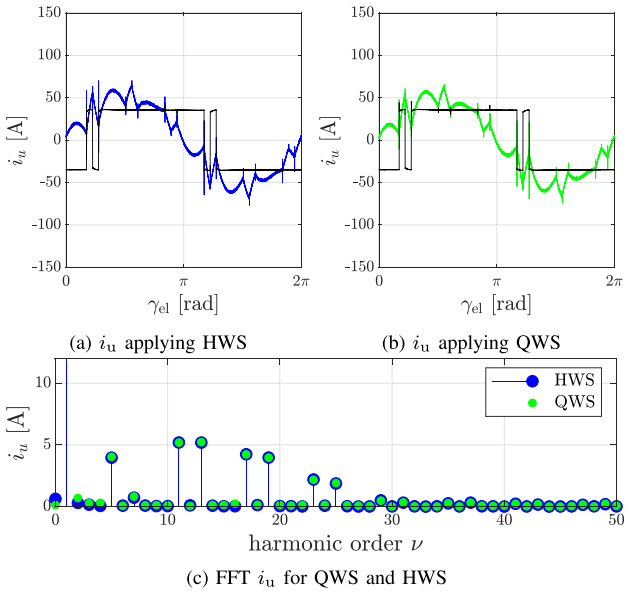

(a) i_u applying HWS (b) i_u applying QWS

(c) FFT i_u for QWS and HWS

FIGURE 24. Measured current waveforms and current FFTs applying QWS and HWS at $m = 1.24$ and $\theta_u = 98.89°$ (30 Nm) and 7000 rpm. Additionally the applied pulse pattern obtained by measurements is displayed (——). These measurements emphasizing the minimal differences at $m = 1.24$ comparing HWS and QWS.

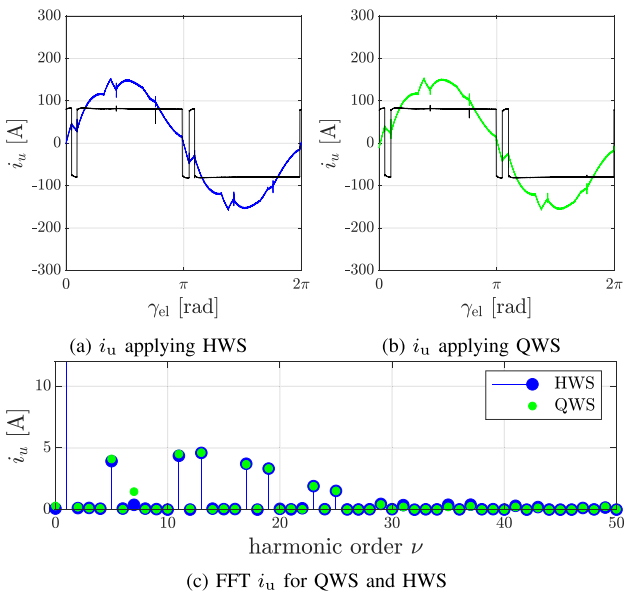

(a) i_u applying HWS (b) i_u applying QWS

(c) FFT i_u for QWS and HWS

FIGURE 25. Measured current waveforms and current FFTs applying QWS and HWS at $m = 1.24$ and $\theta_u = 124.69°$ (120 Nm) and 7000 rpm. Additionally the applied pulse pattern obtained by measurements is displayed (——). These measurements emphasizing the minimal differences at $m = 1.24$ comparing HWS and QWS.

D. EXPERIMENTAL VALIDATION: IMPLEMENTATION STRATEGY OF OPPS

To validate the proposed operating strategy suggested in Section IV-C, based on the accumulated knowledge, various speed-torque points in the operating map of a PMSM are targeted. The base speed range is omitted in this context, as SVPWM is typically employed in this region.

SVPWM with a maximum modulation index of $m_{\max} = 1.15$, OPP with $q = 3$, $m_{\max} = 1.24$ and QWS, as well as six-step modulation is applied. For each operating point in

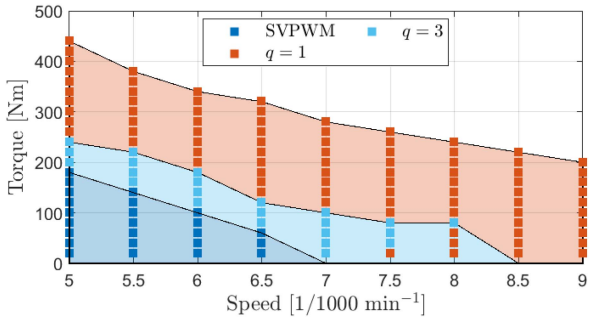

FIGURE 26. Experimental results: optimal outcomes regarding overall efficiency (VSI and PMSM) achieved with SVPWM, $q = 3$ and $q = 1$ across the torque-speed map. The shaded area indicates the practical application where the respective modulation strategy is used to reduce transitions between different pulse numbers.

the torque-speed map, the results with the best efficiency is displayed.

Fig. 26 shows the optimal results for the highest overall efficiency (VSI and PMSM) over all evaluated operating points (indicated by a square ■). The shaded area indicates the practical application where the respective modulation strategy is used to reduce transitions between different pulse numbers.

It is evident that at higher torque levels, six-step operation yields the best results. As the speed increases, the torque threshold at which six-step becomes more efficient than SVPWM or three-pulse switching decreases. This effect is also observed when comparing three-pulse switching to SVPWM.

Three-pulse switching exhibits the best efficiency in the most critical region of the characteristic map, which is at high speeds and low torque levels (long-range highway driving), underscoring the utility of the insights gained from the previous sections.

Statements about actual application usage, when to use $q = 3$, when to use six-step or when to use SVPWM, are difficult to assess. The optimal efficiency achieved through modulation is highly dependent on the specific characteristics of the machine and the inverter. In addition, the DC-link voltage ripple and the torque ripple are strongly influenced by the modulation strategy. This could prevent the use of the most efficient modulation scheme by exceeding application specific limits (e.g. a specified maximum voltage ripple). Especially in six-step operation near the maximum power curve, there is a high probability that these limits will be exceeded.

This experiment was able to confirm the operational strategy proposed in Section IV-C.

VI. CONCLUSION

The performance of electric vehicle drive systems is mainly assessed by efficiency and power density. OPPs can enhance both. In particular, three-pulse switching at very high modulation indexes in the overmodulation region II, is practical for use in automotive microcontrollers.

This work investigates the current distortion in salient PMSMs induced by OPPs, with a focus on three-pulse switching, under various symmetry conditions and in the overmodulation region. The findings can be summarized as follows:

- It is demonstrated analytically and experimentally, that the voltage phase angle θ_u affects current harmonics. At high θ_u, the distortion reduces considerably, also for low pulse numbers or six-step. Thus, switching losses can be reduced while maintaining good current waveform quality.
- Regarding voltage phase angles θ_u close to 90° or 180°, HWS does not show significant advantages compared to QWS. Best results using HWS can be obtained at medium-load operating points having θ_u between 120° and 150°.
- HWS has advantages over QWS in cases where waveforms contain zero-vectors, because the placement of these zero-vectors can be adjusted arbitrarily (linear modulation region). For waveforms that do not contain zero vectors, the advantages of HWS are small (overmodulation region II).
- Based on the results obtained, a practical implementation strategy for OPPs is proposed that leads to the best trade-off between implementation effort and best results in terms of efficiency.
- The solution space for HWS and QWS is carefully studied, and initial angles are selected based on this understanding to increase the likelihood of discovering the global optimum.

REFERENCES

[1] D. G. Holmes and T. A. Lipo, *Pulse Width Modulation for Power Converters: Principles and Practice*, vol. 18. Hoboken, NJ, USA: Wiley, 2003.

[2] M. Hepp et al., "Power electronics for automotive electric drivetrains – Design and optimization," in *Proc. Compon. Power Electron. Appl.*, Bad Nauheim, Germany, 2023, pp. 155–164.

[3] R. Klink, D. Heintges, S. Aleff, R. Scheer, and J. L. Andert, "DENSO's novel development strategy for power electronics and controllers," in *Proc. Aachen Coll. Sustain. Mobil. Aachen, Inst. Automot. Eng.*, Oct. 2021, pp. 1879–1892.

[4] E. Kontodinas, A. Kraemer, H.-D. Endres, S. Wendel, P. Karamanakos, and J. Bonifacio, "An experimental assessment of modulation methods for drive trains used in electric vehicles," in *Proc. 48th Annu. Conf. IEEE Ind. Electron. Soc.*, 2022, pp. 1–6.

[5] K. Douzane, L. Rinehart, C. Keraudren, S. Rodhain, and F. Tahiri, "Inverter and motor efficiency increase with FPCU implementing optimized pulse pattern methods," in *Proc. Int. Electr. Veh. Symp. Exhib.*, Jun. 2021, pp. 1–12.

[6] A. Fathy Abouzeid et al., "Control strategies for induction motors in railway traction applications," *Energies*, vol. 13, no. 3, 2020, Art. no. 700.

[7] T. Velic et al., "Efficiency optimization of electric drives with full variable switching frequency and optimal modulation methods," in *Proc. 17th Conf. Elect. Machines Drives Power Syst. (ELMA)*, 2021, pp. 1–6.

[8] L. Hoelsch et al., "Insights and challenges of co-simulation-based optimal pulse pattern evaluation for electric drives," *IEEE Trans. Energy Convers.*, vol. 39, no. 3, pp. 2094–2105, Sep. 2024.

[9] A. Birda, C. Grabher, C. M. Hackl, and J. Reuss, "DC-link capacitor and inverter current ripples in anisotropic synchronous motor drives produced by synchronous optimal PWM," *IEEE Trans. Ind. Electron.*, vol. 69, no. 5, pp. 4484–4494, May 2022.

[10] M. Gu, Z. Wang, and B. Wang, "Optimization of torque ripple for low-carrier-ratio dual three-phase PMSM with pulse pattern control," *IEEE Trans. Power Electron.*, vol. 38, no. 12, pp. 15091–15096, Dec. 2023.
[11] E. Kontodinas, P. Karamanakos, A. Kraemer, and S. Wendel, "Optimized pulse patterns for anisotropic synchronous machines with improved current and torque properties," in *Proc. 25th Eur. Conf. Power Electron. Appl.*, 2023, pp. 1–8.
[12] I. Koukoula, P. Karamanakos, and T. Geyer, "Optimal pulse width modulation of three-level converters with reduced common-mode voltage," *IEEE Trans. Ind. Appl.*, vol. 60, no. 3, pp. 4062–4075, May/Jun. 2024.
[13] H. El Khatib, D. Gerling, and M. Saur, "Deadbeat flux vector control as a one single control law operating in the linear, overmodulation, and six-step regions with time-optimal torque control," *IEEE Open J. Ind. Appl.*, vol. 3, pp. 247–270, 2022.
[14] A. Brosch, O. Wallscheid, and J. Boecker, "Model predictive control of permanent magnet synchronous motors in the overmodulation region including six-step operation," *IEEE Open J. Ind. Appl.*, vol. 2, pp. 47–63, 2021.
[15] M. Saur, M. Hepp, M. Silva, and W. Wondrak, "Applying DBFC with integrated optimized pulsed pattern to maximize voltage utilization with low distortion in automotive traction drives," in *Proc. 25th Eur. Conf. Power Electron. Appl.*, 2023, pp. 1–9.
[16] V. Zivotic-Kukolj, W. Soong, and N. Ertugrul, "Iron loss reduction in an interior PM automotive alternator," in *Proc. 40th IAS Annu. Meeting. Conf. Rec. Ind. Appl. Conf.*, 2005, pp. 1736–1743.
[17] W. L. Soong, S. H. Han, T. M. Jahns, and N. Ertugrul, "Reducing iron loss in interior pm machines under field-weakening conditions," in *Proc. IEEE Ind. Appl. Annu. Meeting*, 2007, pp. 111–118.
[18] T. Geyer, *Model Predictive Control of High Power Converters and Industrial Drives*. Hoboken, NJ, USA: Wiley, 2016.
[19] Z. Zhang, X. Ge, Z. Tian, X. Zhang, Q. Tang, and X. Feng, "A PWM for minimum current harmonic distortion in metro traction PMSM with saliency ratio and load angle constrains," *IEEE Trans. Power Electron.*, vol. 33, no. 5, pp. 4498–4511, May 2018.
[20] N. Hartgenbusch, R. W. De Doncker, and A. Thünen, "Optimized pulse patterns for salient synchronous machines," in *Proc. 23rd Int. Conf. Elect. Machines Syst. (ICEMS)*, 2020, pp. 359–364.
[21] A. Birda, J. Reuss, and C. M. Hackl, "Synchronous optimal pulsewidth modulation for synchronous machines with highly operating point dependent magnetic anisotropy," *IEEE Trans. Ind. Electron.*, vol. 68, no. 5, pp. 3760–3769, May 2021.
[22] G. Darivianakis and I. Tsoumas, "Insight into the peculiarities of optimized pulse patterns for permanent-magnet synchronous machines," in *Proc. 22nd Eur. Conf. Power Electron. Appl.*, 2020, pp. P.1–P.8.
[23] E. Kontodinas, P. Karamanakos, A. Kraemer, and S. Wendel, "Optimized pulse patterns for synchronous machines with non-sinusoidal back-EMF," in *Proc. 25th Eur. Conf. Power Electron. Appl.*, 2023, pp. 1–9.
[24] O. Karaca and I. Tsoumas, "Robust optimized pulse patterns for salient permanent magnet synchronous machines," in *Proc. 25th Eur. Conf. Power Electron. Appl.*, 2023, pp. 1–9.
[25] M. Hepp, M. Saur, W. Wondrak, and M.-M. Bakran, "Optimized pulse patterns for salient permanent magnet synchronous machines considering nonlinear magnetic effects," in *Proc. Int. Exhib. Conf. Power Electron., Intell. Motion Renewable Energy Energy Manage.*, 2023, pp. 1–10.
[26] A. Tripathi and G. Narayanan, "High-performance off-line pulse width modulation without quarter wave symmetry for voltage-source inverter," in *Proc. Int. Conf. Adv. Electron. Comput. Commun.*, 2014, pp. 1–6.
[27] A. Tripathi and G. Narayanan, "Optimal pulse width modulation of voltage-source inverter fed motor drives with relaxation of quarter wave symmetry condition," in *Proc. IEEE Int. Conf. Electron. Comput. Commun. Technol. (CONECCT)*, 2014, pp. 1–6.
[28] A. Birth, T. Geyer, and H. du Toit Mouton, "Symmetry relaxation of three-level optimal pulse patterns for lower harmonic distortion," in *Proc. 21st Eur. Conf. Power Electron. Appl.*, 2019, pp. P.1–P.10.
[29] A. Birth, T. Geyer, H. D. T. Mouton, and M. Dorfling, "Generalized three-level optimal pulse patterns with lower harmonic distortion," *IEEE Trans. Power Electron.*, vol. 35, no. 6, pp. 5741–5752, Jun. 2020.
[30] W. Zheng, Y. Zhang, and Y. Wang, "Synchronized SVPWM with half-wave symmetry relaxation for low-switching-frequency three-level NPC inverter," in *Proc. IEEE Int. Conf. Predictive Control Elect. Drives Power Electron. (PRECEDE)*, 2023, pp. 1–6.
[31] A. D. Birda, J. Reuss, and C. Hackl, "Synchronous optimal pulse-width modulation with differently modulated waveform symmetry properties for feeding synchronous motor with high magnetic anisotropy," in *Proc. 19th Eur. Conf. Power Electron. Appl.*, 2017, pp. P.1–P.10.
[32] *MathWorks*, "Optimization toolbox user's guide," 2023, [Online]. Available: https://de.mathworks.com/help/pdf_doc/optim/optim.pdf
[33] F. Jenni and D. Wüest, *Steuerverfahren für Selbstgeführte Stromrichter*. Zürich, Switzerland: vdf Hochschulverlag AG, 1995.
[34] G. Konstantinou and V. Agelidis, "On re-examining symmetry of two-level selective harmonic elimination PWM: Novel formulations, solutions and performance evaluation," *Electric Power Syst. Res.*, vol. 108, pp. 185–197, 2014.
[35] K. Peter, J. Böcker, F. Mink, and S. Beineke, "Comparison of quarter-wave with half-wave symmetrical pulse patterns applied in electrical high-speed drives," in *Proc. 8th IET Int. Conf. Power Electron. Machines Drives*, 2016, pp. 1–6.
[36] G. S. Konstantinou and V. G. Agelidis, "Bipolar switching waveform: Novel solution sets to the selective harmonic elimination problem," in *Proc. IEEE Int. Conf. Ind. Technol.*, 2010, pp. 696–701.
[37] S. L. Kellner and B. Piepenbreier, "General PMSM d,q-model using optimized interpolated absolute and differential inductance surfaces," in *Proc. IEEE Int. Electric Machines Drives Conf. (IEMDC)*, 2011, pp. 212–217.
[38] Y.-C. Kwon, S. Kim, and S.-K. Sul, "Six-step operation of PMSM with instantaneous current control," *IEEE Trans. Ind. Appl.*, vol. 50, no. 4, pp. 2614–2625, Jul./Aug. 2014.
[39] L. Wachter, O. Karaca, G. Darivianakis, and T. Charalambous, "A convex relaxation approach for the optimized pulse pattern problem," in *Proc. Eur. Control Conf. (ECC)*, 2021, pp. 2213–2218.
[40] A. K. Vijayan, D. Xiao, B. Batkhishig, A. D. Callegaro, R. Baranwal, and A. Emadi, "Comparative study on pulse pattern optimization for high-speed permanent magnet synchronous motors," in *Proc. IEEE Transp. Electrific. Conf. Expo (ITEC)*, 2022, pp. 708–713.
[41] M. Hepp, K. Kaiser, M. Saur, W. Wondrak, and M.-M. Bakran, "Implementation and control of optimized pulse patterns for salient permanent magnet synchronous machines in electric vehicles," in *Proc. Int. Exhib. Conf. Power Electron. Intell. Motion Renewable Energy Energy Manage.*, Nürnberg, Germany, 2024, pp. 3040–3054.

MAXIMILIAN HEPP was born in Germany, in 1990. He received the Diploma in mechanical engineering from the University of Applied Sciences Wuerzburg-Schweinfurt, Schweinfurt, Germany, in 2015, and the M.Sc. degree in mechanical engineering from the University of Stuttgart, Stuttgart, Germany, in 2018. He is currently with the Power Electronics Advanced Engineering Department, Mercedes-Benz AG, Boeblingen, Germany. His research interests include control of electrical machines and inverter technology.

KIM KAISER was born in Germany, in 1998. She received the B.Sc. degree in electrical engineering and information technology in 2021 from the University of Stuttgart, Stuttgart, Germany, where she is currently working toward the M.Sc. degree. Her research interests include control systems, electric drives, and power electronics in automotive applications.

MICHAEL SAUR received the B.Eng. degree in electrical engineering from the University of Applied Sciences Esslingen, Esslingen am Neckar, Germany, in 2011, the M.Sc. degree in electrical engineering from the University of Erlangen/Nuremberg, Erlangen, Germany, in 2013, and the Dr.-Ing. degree from the Universitaet der Bundeswehr Muenchen, Neubiberg, Germany, in 2016. From 2017 to 2021, he was with the Research and Development Department, Audi AG, Ingolstadt, Germany. In 2022, he joined the Power Electronics Advanced Engineering Group, Mercedes-Benz AG, Boeblingen, Germany, and is currently working on innovative technologies for next generation battery electric vehicles.

MARK-M. BAKRAN (Senior Member, IEEE) received the Diploma and Dr.-Ing. degrees in electrical engineering from the Technical University of Berlin, Berlin, Germany, in 1992 and 1995, respectively. From 1995 to 2011, he was with Siemens AG, Berlin. Within the Traction Division, he was responsible for power electronics from auxiliary converters to hybrid buses and from light rail vehicles to locomotives. In 2011, he became an Appointed Professor with the University of Bayreuth, Bayreuth, Germany.